

See discussions, stats, and author profiles for this publication at: <https://www.researchgate.net/publication/235680271>

# Interfacial Characteristics of a PEGylated Imidazolium Bistriflamide Ionic Liquid Electrolyte at a Lithium Ion Battery Cathode of $\text{LiMn}_2\text{O}_4$

ARTICLE in ACS APPLIED MATERIALS & INTERFACES · FEBRUARY 2013

Impact Factor: 6.72 · DOI: 10.1021/am302921r

CITATIONS

6

READS

79

5 AUTHORS, INCLUDING:



**Simon E. Rock**

Clarkson University

11 PUBLICATIONS 67 CITATIONS

SEE PROFILE



**Sitaraman Krishnan**

Clarkson University

69 PUBLICATIONS 1,528 CITATIONS

SEE PROFILE



**Dipankar Roy**

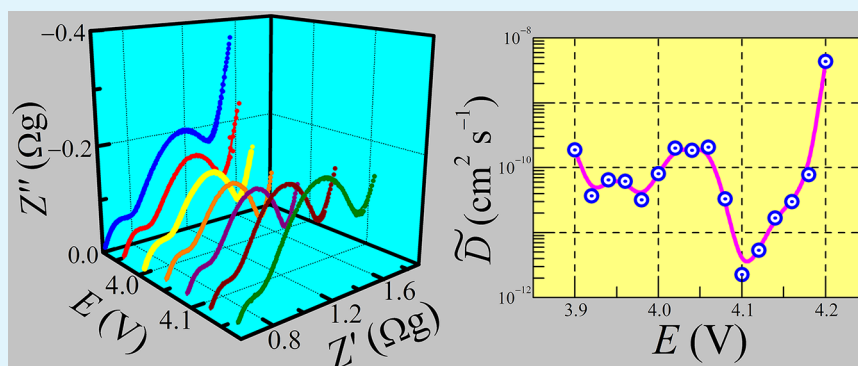
Clarkson University

131 PUBLICATIONS 2,545 CITATIONS

SEE PROFILE

Interfacial Characteristics of a PEGylated Imidazolium Bistriflamide Ionic Liquid Electrolyte at a Lithium Ion Battery Cathode of  $\text{LiMn}_2\text{O}_4$ Simon E. Rock,<sup>†</sup> Lin Wu,<sup>‡</sup> Daniel J. Crain,<sup>†</sup> Sitaraman Krishnan,<sup>‡</sup> and Dipankar Roy<sup>\*,†</sup><sup>†</sup>Department of Physics and <sup>‡</sup>Department of Chemical and Biomolecular Engineering, Clarkson University, Potsdam, New York 13699, United States

## S Supporting Information



**ABSTRACT:** Nonvolatile and nonflammable ionic liquids (ILs) have distinct thermal advantages over the traditional organic solvent electrolytes of lithium ion batteries. However, this beneficial feature of ILs is often counterbalanced by their high viscosity (a limiting factor for ionic conductivity) and, sometimes, by their unsuitable electrochemistry for generating protective layers on electrode surfaces. In an effort to alleviate these limiting aspects of ILs, we have synthesized a PEGylated imidazolium bis(trifluoromethylsulfonyl)amide (bistriflamide) IL that exhibited better thermal and electrochemical stability than a conventional electrolyte based on a blend of ethylene carbonate and diethyl carbonate. The electrochemical performance of this IL has been demonstrated using a cathode consisting of ball-milled  $\text{LiMn}_2\text{O}_4$  particles. A direct comparison of the ionic liquid electrolyte with the nonionic low-viscosity conventional solvent blend is presented.

**KEYWORDS:** cathode interface, energy storage material, lithium ion battery, impedance spectroscopy, ionic liquid electrolyte, voltammetry

## ■ INTRODUCTION

The volatile and flammable electrolytes commonly used in Li ion batteries tend to restrict the utility of such batteries at elevated temperatures. Recent developments in ionic liquid (IL) electrolytes provide an effective approach to addressing this issue, because ILs are essentially nonflammable and have negligible vapor pressure.<sup>1–5</sup> However, systematic incorporation of neat ILs in Li ion battery electrolytes still remains a challenging task, and the specific factors for consideration in this regard are the viscosity, compatibility with electrode chemistries, and solid-electrolyte interphase (SEI) forming capability of ILs. SEI-forming solvents are often incorporated in IL based electrolytes,<sup>6,7</sup> where the viscosity-lowering properties of the solvents additionally facilitate  $\text{Li}^+$  conduction.<sup>6–9</sup> Depending on the system, however, this approach can bring back some of the thermal disadvantages of organic solvents.

To fully utilize the functionalities of an IL electrolyte in Li-ion or Li-metal batteries, the design of the IL should include not only the considerations of conductivity and thermal stability, but also those of electrode–electrolyte interfacial characteristics.<sup>1,8,9</sup> With high voltage cathodes such as

$\text{LiMn}_2\text{O}_4$ ,  $\text{LiCoPO}_4$ , and  $\text{LiNi}_{0.5}\text{Mn}_{1.5}\text{O}_4$ , the maximum operating cell voltage is chiefly determined by the electrochemical stability of the electrode–electrolyte interface.<sup>10</sup> Similarly, the power output of the battery could be affected by the resistance of the electrolyte film formed on the electrode surface and the rates of  $\text{Li}^+$  insertion/extraction at the cathode/anode.<sup>8,11</sup> The present work addresses these specific issues by using a  $\text{Li}^+$  conductive PEGylated imidazolium bistriflamide IL, [mPEG7MeIm][Tf<sub>2</sub>N].

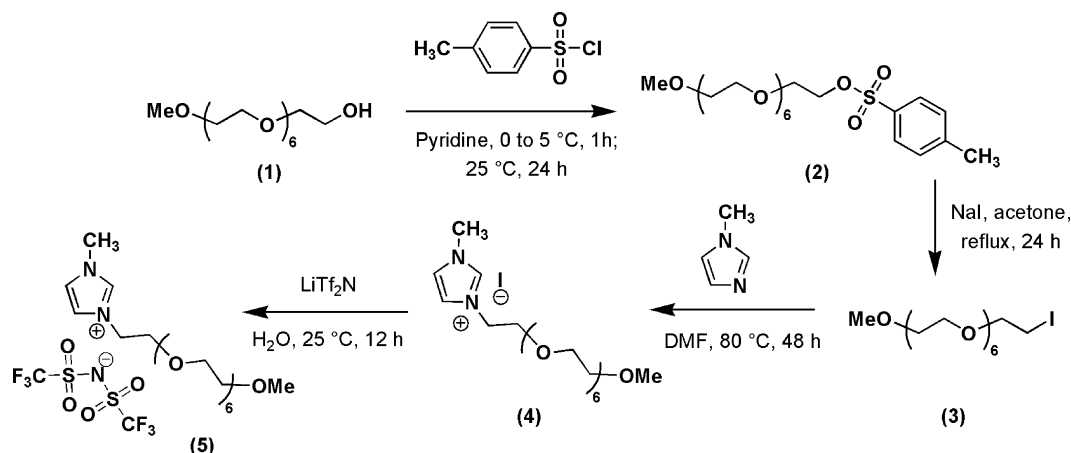
The factors that motivated the design of the specific PEG-functionalized IL for our present study are as follows. The PEG module of this IL has several attractive features as an efficient electrolyte component of Li ion batteries.<sup>12–14</sup> These include its robust faradaic stability, its ability to adequately dissolve Li salts (a beneficial outcome of the complexing ability of the polymer's ether oxygen atoms with cations), and a plasticizing effect that promotes ionic conduction. Furthermore, the

Received: December 7, 2012

Accepted: February 22, 2013



Scheme 1. Synthesis of PEGylated Imidazolium Bistriflamide IL



inclusion of PEG in an IL can effectively screen the anion–cation Coulombic interactions and hence can increase the fluidity (ionic conductivity) of the IL. This particular feature of PEG has been demonstrated for the PEGylated methylimidazolium iodide ILs, [mPEG $n$ MeIm]I, with 7, 12, and 16 oxygen atoms in the PEG tail.<sup>12</sup> Despite their polymeric nature, these ILs can exhibit considerable fluidity and ionic conductivity, as their PEG tail of the cation engages in hydrogen-bonding interactions with the imidazolium ring, and consequently screens the viscosity promoting ionic interactions in the IL.

The choice of LiTf<sub>2</sub>N, with the highly charge-delocalized bistriflamide ([Tf<sub>2</sub>N]<sup>−</sup>) anion, is also based on the weakening of anion–cation interactions,<sup>15</sup> thereby enhancing salt dissociation and increasing electrolyte conductivity. However, a potential problem with the fluorinated Li salt is that it would have limited solubility in both polar PEGylated and nonpolar alkylated compounds (because fluorinated groups are generally immiscible with PEG and alkyl groups).<sup>16,17</sup> Conversely, most Li salts tend to be poorly soluble in ILs with fluorinated anions.<sup>18,19</sup> We avoided these solubility issues by using a PEGylated imidazolium IL with the same anion as that of the LiTf<sub>2</sub>N salt. The common [Tf<sub>2</sub>N]<sup>−</sup> anion shared by the IL and the salt helps the dissolution and dissociation of the salt in the IL, prevents the formation of ionic clusters, and thus enhances Li<sup>+</sup> conductivity of the IL electrolyte.

With a selected set of experimental probes, we demonstrate here how the proposed design of [mPEG7MeIm][Tf<sub>2</sub>N] can contribute to the strategies currently used<sup>1</sup> in the development of such ILs for battery-specific applications. This report describes the synthesis scheme of [mPEG7MeIm][Tf<sub>2</sub>N], along with results for the IL's conductivity and thermal stability. The battery specific interfacial electrochemistry of 1 M LiTf<sub>2</sub>N in [mPEG7MeIm][Tf<sub>2</sub>N] is examined with slow scan cyclic voltammetry (SSCV)<sup>8,9,20</sup> at room temperature by using a cathode of lithium manganese oxide (LMO) spinel in a half-cell with a Li anode. These SSCV results are compared with those recorded under similar conditions using a control electrolyte of 1 M LiTf<sub>2</sub>N in a conventional mixed solvent (1:1 by volume) of ethylene carbonate (EC) and diethyl carbonate (DEC). Scheme 1 depicts the reactions used for the synthesis of the bistriflamide IL, 5, using the iodide precursor, 4, obtained through our previously reported approach.<sup>12</sup>

## RESULTS AND DISCUSSION

**Thermal Stability and Ionic Conductivity.** The results shown in Figure 1 demonstrate the thermal benefits of the

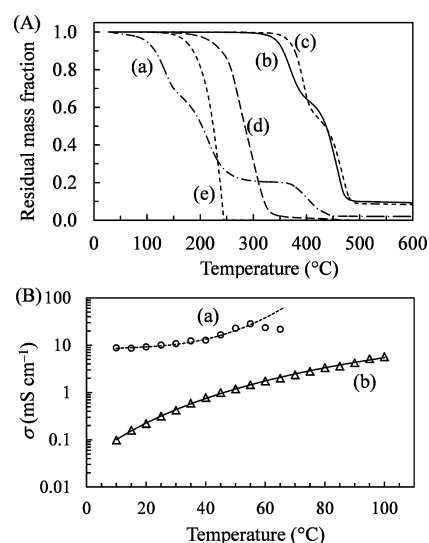


**Figure 1.** (A) Thermogravimetric plots for: (a) 1 M solution of LiTf<sub>2</sub>N in 1:1 EC/DEC blend, (b) 1 M solution of LiTf<sub>2</sub>N in [mPEG7MeIm][Tf<sub>2</sub>N], (c) [mPEG7MeIm][Tf<sub>2</sub>N] IL, (d) mPEG precursor 1 (Scheme 1), and (e) tetraglyme. (B) Conductivity plots for electrolytes a and b considered in part A.

PEGylated IL electrolyte. In Figure 1A, the IL system represented by the thermogravimetric plots b and c is noticeably more stable than its EC/DEC counterpart in plot a. Evaporative mass loss of the EC/DEC electrolyte begins well below 100 °C and increases drastically at higher temperatures. In contrast, the IL electrolyte remains thermally stable up to about 350 °C. The thermal stability of the IL is also substantially superior to those of monomethoxy-terminated PEG (cf. curve d in Figure 1A) and tetraglyme (cf. curve e), which are often used as solvents in lithium ion batteries. A comparison of plots c and d shows how ionicity enhances thermal stability of PEGylated compounds.

Figure 1B compares the ionic conductivities of the [mPEG7MeIm][Tf<sub>2</sub>N] and EC/DEC electrolytes. The symbols denote experimental data, and the line b is a calculated fit using the Vogel–Fulcher–Tammann equation:<sup>15</sup>  $\ln(\sigma/\text{mS})$

$\text{cm}^{-1}) = 5.6386 - 3.6268/[(T/194.29) - 1]$ , where the numbers represent the values of the parameter in the equation,  $\sigma$  is the IL's conductivity, and  $T$  is the absolute temperature. The high ionic conductivity of the EC/DEC solvent blend is supported by the lower viscosity of the blend. However, the EC/DEC electrolyte shows significant evaporation in the conductivity cell at  $T > 50^\circ\text{C}$ , which introduces large uncertainties in the data recorded at higher temperatures.

For a comparative assessment of the data in Figure 1B, we note that at room temperature, the ionic conductivity of the EC/DEC electrolyte is  $10.08 \text{ mS cm}^{-1}$  and that most PEG-IL electrolytes are significantly less conductive.<sup>1</sup> At  $25^\circ\text{C}$ , the ionic conductivity values published for PEG-IL electrolytes generally are limited to at least 2 orders of magnitude below the aforementioned value for EC/DEC,<sup>21,22</sup> while only a few systems have been found so far to overcome this limit (but not tested for battery-specific interfacial electrochemistry).<sup>13,23</sup> The conductivity of  $[\text{mPEG7MeIm}][\text{Tf}_2\text{N}]$  found from Figure 1B at  $25^\circ\text{C}$  is  $0.32 \text{ mS cm}^{-1}$ . This result can be compared with the room temperature conductivity of IL-nanoparticle hybrid electrolytes ( $\approx 0.1 \text{ mS cm}^{-1}$ )<sup>24</sup> or that of the poly(3-hexylthiophene)-*b*-poly(ethylene oxide) block copolymer electrolyte ( $\approx 0.1 \text{ mS cm}^{-1}$ )<sup>25</sup> recently developed for lithium ion batteries.

At  $T \leq 50^\circ\text{C}$ , the ionic conductivity of the EC/DEC system follows the empirical equation  $\ln(\sigma/\text{mS cm}^{-1}) = 469.37 - 3341.82x + 7979.11x^2 - 6359.35x^3$ , where  $x = 1000/RT$  and  $R$  is the gas constant.<sup>12</sup> The line plot in Figure 1B shows a fit to the lower-temperature data according to this equation. The EC/DEC electrolyte has a notably lower activation energy of conductivity ( $8.86 \text{ kJ mol}^{-1}$  at  $25^\circ\text{C}$ , compared with  $48.28 \text{ kJ mol}^{-1}$  for the IL electrolyte at the same temperature). The activation energies,  $E_a$ , were calculated in the conventional approach by using the formula:  $E_a = RT^2 d(\ln \sigma)/dT$ .<sup>15,26</sup> Despite its overall higher conductivity, the utility of the EC/DEC system remains limited to the lower temperature region, whereas the IL behaves uniformly in the entire temperature range explored.

**Temperature Dependent Electrochemical Windows of  $[\text{mPEG7MeIm}][\text{Tf}_2\text{N}]$  and  $[\text{EC/DEC}][\text{Tf}_2\text{N}]$  Electrolytes.** The experimental considerations for measuring electrochemical windows (EWs) of ILs by using CV have been discussed elsewhere in detail.<sup>27,28</sup> To determine the voltage thresholds of the cathodic and anodic reactions (limits of the EW, respectively), it is usually necessary to extend the scan-voltage of CV well beyond the nonfaradaic bounds of the given system. Rapid voltage scans are useful for these measurements, as they minimize electrolyte degradation due to cumulative faradaic reactions while probing through electrode potentials outside the EW. Furthermore, kinetically controlled voltammetric currents of the electroactive species adsorbed on an electrode are proportional to the voltage scan speed ( $v$ ).<sup>29</sup> Therefore, relatively high voltage sweep rates of  $50\text{--}200 \text{ mV s}^{-1}$  are frequently used to promote the detection of these currents in EW measurements for ILs.<sup>28,30–33</sup>

On the basis of these facts, and to avoid excessive double layer currents at the same time, we used a moderately fast sweep rate of  $50 \text{ mV s}^{-1}$  to determine the EWs of the experimental electrolytes at a glassy carbon (GC) electrode. Figure 2 shows the resulting voltammograms, recorded at (a)  $25^\circ\text{C}$ , (b)  $45^\circ\text{C}$ , and (c)  $65^\circ\text{C}$  in the  $\text{LiTf}_2\text{N}$  electrolytes of (A) EC/DEC and (B) IL. In general, the overall voltage range necessary to evaluate the EW of a given system is largely determined by

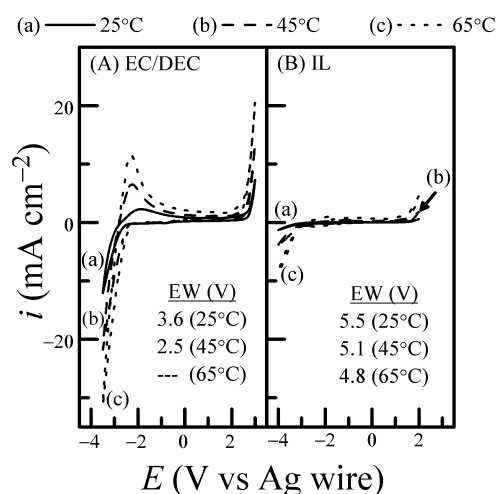


**Figure 2.** Comparison of temperature dependent electrochemical windows for (A) 1 M solution of  $\text{LiTf}_2\text{N}$  in 1:1 EC/DEC blend and (B) 1 M solution of  $\text{LiTf}_2\text{N}$  in  $[\text{mPEG7MeIm}][\text{Tf}_2\text{N}]$ , using a glassy carbon electrode. The electrolyte temperatures used are (a)  $25^\circ\text{C}$ , (b)  $45^\circ\text{C}$ , and (c)  $65^\circ\text{C}$ .

the electrochemical activities of the salt and the background component of the electrolyte (e.g.,  $\text{LiTf}_2\text{N}$  and PEG in Figure 2, respectively).<sup>27,30–32</sup> The voltage scan range in Figure 2 was set according to these criteria.

The EC/DEC electrolyte begins to oxidize at  $E \geq 2.5 \text{ V}$ , leading to the related sharply rising anodic currents. Similarly, this electrolyte undergoes electro-reduction at  $E \leq -2.5 \text{ V}$ , resulting in the rather large cathodic current features observed at the negative voltages in Figure 2A. The smaller anodic current peaks observed between  $-0.25$  and  $-0.20 \text{ V}$  during the positive voltage scans in Figure 2 represent electro-oxidation of the species reduced in the negative scan. These oxidation and reduction processes become more intense with increasing temperatures, as indicated by their correspondingly increasing faradaic features.

Within the voltage region scanned to locate the EW, some background currents typically arise from double layer effects and sometimes from electro-active impurities in the electrolyte. Thus, an EW formally refers to the potential region where the currents are relatively insignificant but not necessarily zero,<sup>27</sup> and the data shown in Figure 2 correspond to this situation. A cutoff current of  $1.5 \text{ mA cm}^{-2}$  has been previously reported for typical EWs of GC-IL systems.<sup>28</sup> On the basis of this value, the temperature dependent EWs of the EC/DEC and the IL electrolytes are noted in Figure 2A and B, respectively.

The potential energy barriers of the faradaic reactions occurring outside the EWs are lowered as the sample temperatures are increased. Due to this reason, the EWs for both sets of electrolytes decrease with increasing temperatures. At all the three temperatures explored here, the IL has a noticeably wider EW compared to that of the EC/DEC electrolyte, and this difference between the two electrolytes increases with increasing temperatures. Specifically, the widely recognized cathodic instability of imidazolium based ILs<sup>6</sup> is largely controlled in the present case, evidently because of the interaction of protons in the imidazolium ring with oxygen atoms in the PEG tail.<sup>12</sup> At  $65^\circ\text{C}$ , the currents measured throughout the scanned voltage zone for the EC/DEC system is higher than  $1.5 \text{ mA cm}^{-2}$ . As a result, the EW current cutoff used here does not allow for choosing a finite stability window



in this case. Additional data presented in the Supporting Information suggests that the overall EW of the IL is controlled predominantly by the faradaic stability of the IL's PEG module.

**Slow Scan Cyclic Voltammetry of LMO/IL/Li Cells.** The charge capacities of typical Li ion batteries are cathode limited. For example, the theoretical charge capacity of  $148.2 \text{ mAh g}^{-1}$  of a  $\text{LiMn}_2\text{O}_4$  cathode is significantly lower than the value of  $372 \text{ mAh g}^{-1}$  of a carbon anode. Therefore, a cathode material is chosen here to evaluate the interfacial electrochemistry of the PEGylated IL. The specific choice of an LMO cathode in this work is guided by the observation that LMO shows rather distinct voltammetric signatures of Li intercalation/deintercalation.<sup>9,34</sup> These SSCV features of LMO serve as a marker of the voltage-dependent phase compositions of the Li host lattice and also provide a measure of the electrolyte's interactions with the host particles. Moreover, the relatively high electrode potential of  $\text{LiMn}_2\text{O}_4$  versus lithium ( $\approx 4 \text{ V}$ ) provides an additional metric for evaluating the electrochemical stability of the PEGylated IL electrolyte.

The LMO particles used in this work were mechanochemically processed following a specific procedure of ball milling described in our earlier reports.<sup>9,20</sup> The active material obtained in this approach is found in a bimodal distribution of micrometric and nanometric particles, and the electrochemical characteristics of these mixed particles have been studied in detail.<sup>9</sup> Since the cathode-specific electrochemical effects of this type of ball-milled LMO are now reasonably established,<sup>9,20,35,36</sup> an electrode fabricated using these particles facilitates the task of probing the performance characteristics of the new IL electrolyte reported herein.

Figure 3 shows SSCV results, comparing the general electrochemical features of the IL and the EC/DEC electrolytes. Plots a and b in panel A were recorded with an LMO working electrode at a voltage scan speed,  $v$ , of  $100 \mu\text{V s}^{-1}$ , by using the EC/DEC and IL electrolytes, respectively. The fresh electrode was first scanned anodically (Li extraction), followed by a corresponding cathodic scan (Li insertion), and this process was repeated several times. The data from the second scan was used for Figure 3 to minimize the initial contributions of SEI formation to the Li extraction/insertion currents.<sup>8</sup>

In plot a of Figure 3A, the current peaks for anodic deintercalation of Li from the cathode ( $\text{LiMn}_2\text{O}_4 \rightarrow \text{Li}_{1-x}\text{Mn}_2\text{O}_4 + x\text{Li}^+ + xe^-$ ) are labeled as  $P_{a1}$  and  $P_{a2}$  while the corresponding cathodic features are marked as  $P_{c1}$  and  $P_{c2}$ . The current peaks in the SSCV plots correspond to different phases of  $\text{Li}_y\text{Mn}_2\text{O}_4$  spinels formed by changes in Li concentrations during extraction or insertion. X-ray diffraction studies<sup>37</sup> have shown the existence of a single phase, A ( $\lambda\text{-MnO}_2$  solid solution), in the composition range of  $y = 0\text{--}0.10$ , the coexistence of a lithium-poor phase, A, and a lithium-rich phase, B, in the range of  $y = 0.10\text{--}0.35$ , a single-phase solid solution, B, in the range of  $y = 0.35\text{--}0.5$ , and another single-phase solid solution, C, above  $y = 0.5$ .  $P_{a1}$  has been associated with the  $C \rightarrow B$  phase transition, and  $P_{a2}$  has been associated with the  $B \rightarrow A$  transition.<sup>8,9,37</sup>

At  $v = 100 \mu\text{V s}^{-1}$ , the current peaks in Figure 3A are well-defined for the EC/DEC system but barely resolved for the IL. The positions of these current features (largest current amplitudes) in the latter case are indicated by the vertical arrows associated with plot b. For the IL, a sizable lowering of  $v$  was necessary to fully resolve these current peaks. This is demonstrated in Figure 3B, where the displayed voltammogram was collected in the IL using  $v = 5 \mu\text{V s}^{-1}$ .

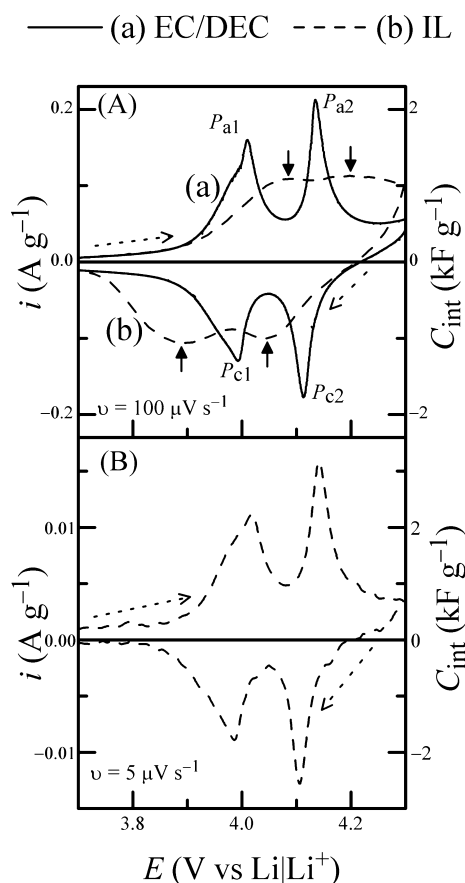


**Figure 3.** SSCV of LMO cathodes, recorded using 1 M solutions of  $\text{LiTf}_2\text{N}$  in a 1:1 mixture of EC and DEC [plot a in A], and  $[\text{mPEG7MeIm}][\text{Tf}_2\text{N}]$  [plot b in A and the plot in B]. The left and the right axes show the voltammetric currents ( $i$ ) and the intercalation capacitances ( $C_{\text{int}} = i/v$ ), respectively, both normalized with respect to the active material mass. The dotted arrows show the direction of voltage scan.

Figure 4A shows the observed peak currents for the three SSCV systems considered in Figure 3. Figure 4B shows the difference,  $\Delta E_p$ , measured between the voltage positions of the anodic and cathodic occurrences of a given current peak. This  $\Delta E_p$  represents the extent of voltage polarization, which, for the IL increases noticeably as  $v$  increases from 5 to  $100 \mu\text{V s}^{-1}$  in going from systems III to II. The origin of such scan rate dependent polarization effects of SSCV has been extensively studied for Li intercalation systems<sup>34,38,39</sup> and, based on these earlier studies, can be largely associated with diffusion effects due to concentration gradients of  $\text{Li}^+$  developed between the surface and the core regions of the active particle during intercalation/deintercalation.

While  $\Delta E_p$  for the LMO-IL system II in Figure 4B implies the presence of diffusion limited Li transport, under similar conditions of SSCV ( $v < 90 \mu\text{V s}^{-1}$ ), Li transport in the LMO-EC/DEC cell is not diffusion-limited.<sup>9</sup> According to previously reported results,<sup>34,38–42</sup> this suggests that the voltage polarization,  $\Delta E_p$ , observed in the IL system II is governed mostly by a surface film consisting of covalently bound as well as physically adsorbed IL molecules on the LMO particle surface. This film, generally referred to as the solid electrolyte interphase (SEI) has a significantly higher resistance than the SEI formed in the EC/DEC system (discussed later in the section on impedance spectroscopy). Evidently, a strong

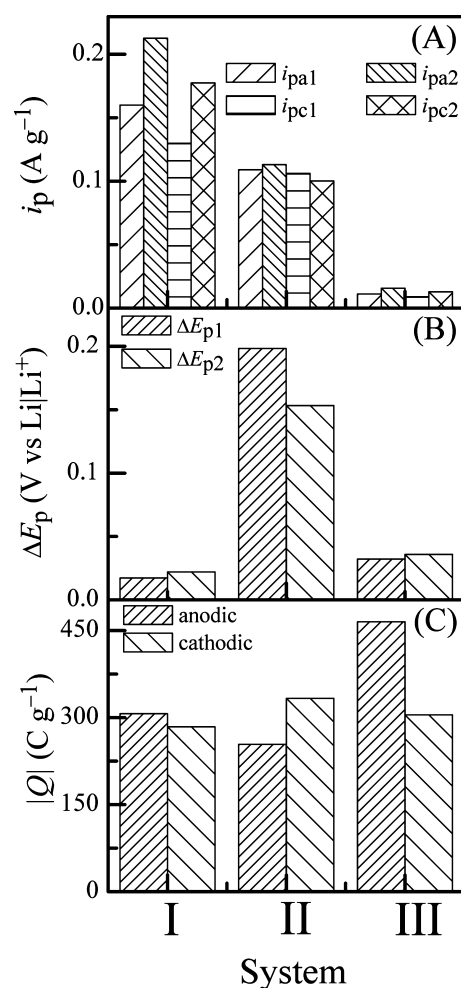


**Figure 4.** Parameters obtained from the voltammograms of Figure 3. Systems I, II, and III represent the EC/DEC electrolyte with  $\nu = 100 \mu\text{V s}^{-1}$ , IL electrolyte with  $\nu = 100 \mu\text{V s}^{-1}$ , and IL electrolyte with  $\nu = 5 \mu\text{V s}^{-1}$ , respectively. (A) Peak currents,  $i_p$ . (B) Voltage gaps,  $\Delta E_p$ , between the positions of the anodic and cathodic current peaks. (C) Integrated gravimetric charges due to anodic deintercalation and cathodic intercalation of Li in LMO.

gradient of  $\text{Li}^+$  concentration exists in the SEI film of system II, wherein a faster scan rate of  $100 \mu\text{V s}^{-1}$  is employed.<sup>34,38</sup> In contrast, the gradient is weaker in system III when a significantly lower scan rate of  $5 \mu\text{V s}^{-1}$  is used. Hence, voltage polarization in system III is almost as low as that in the EC/DEC system I, which is associated with a significantly less resistive SEI film. According to these observations, the diffusion limitation of  $\text{Li}^+$  transport detected by SSCV occurs mainly in the SEI rather than in the active host particle itself.

**Peak Broadening.** The observed broadening of the SSCV current peaks for system II can be explained in terms of an interacting lattice model, as discussed in the Supporting Information. The widths of the voltammetric current peaks due to extraction/insertion of Li in the LMO particles depend on the strength and the nature of nearest neighbor interactions within the host lattice.<sup>43</sup> During fast charge/discharge, the Li concentration in the particle becomes inhomogeneous, and the specific area of the particle plays a governing role in Li extraction/insertion.<sup>44,45</sup> The voltammetric signature of these effects is prominently manifested at high scan rates when the

distribution of Li in the individual host particles is most inhomogeneous.

**Active Material Utilization.** The extent of active material utilization is an important factor that determines the charge capacity of a lithium ion battery.<sup>9</sup> The internal mass transfer resistance of the LMO particles could lower the charge capacity of the battery, particularly with particles of large diameters, as has been explained previously by using a the “shrinking-core” model for Li extraction or insertion.<sup>46</sup> In the presence of large internal mass transfer resistance, the state of charge (SoC),  $x$ , defined as the fraction of lattice sites in the host particle available for intercalating Li, varies between the core and surface regions of the particle.<sup>44,46</sup> The SoC,  $x$ , is equal to 0 in the fully discharged state and equal to 1 in the fully charged state.

If the SoC of an LMO particle has a value of  $x_s$  at the particle surface and a different value  $x_c$  in the core, the degree of active material utilization is largely determined by the charge/discharge rate dependent values of  $|x_s - x_c|$  and, hence, by that of  $\nu$  in SSCV. During charging, if the cathode potential is increased rapidly to the maximum value of 4.3 V (vs  $\text{Li|Li}^+$ ),  $x_s$  quickly approaches its maximum value of 1 while  $x_c$  is still below 1. Thus, the core of the active particle remains underutilized.<sup>44</sup>

Figure 4C examines the above consideration of material utilization in the LMO/IL/Li cell by comparing the cumulative faradaic charge magnitudes,  $|Q|$ , of Li extraction/insertion, obtained by integrating the areas under the SSCV current peaks. The baseline for integration was set at the level of the double layer current detected at the cathodic end of the CV scan. The anodic charge densities plotted in Figure 4C represent the quantity,  $xQ_m$ , where  $x$  is the spatially averaged SoC of the entire LMO electrode measured at the end of a charge cycle and  $Q_m$  is the maximum available value of the charge capacity of the electrode. The theoretical capacity of  $\text{LiMn}_2\text{O}_4$  (molar mass =  $180.81 \text{ g mol}^{-1}$ ) is about  $148.2 \text{ mAh g}^{-1}$  ( $533.6 \text{ C g}^{-1}$ ). On the basis of this maximum available value of  $Q_m$ , and the experiment charge density of about  $300 \text{ C g}^{-1}$ , the value of  $x$  for both the EC/DEC and IL cells is estimated to be about 0.6. It should be noted that the theoretical capacity of ball-milled LMO is lower than the value of  $148.2 \text{ mAh g}^{-1}$  based on the  $\text{LiMn}_2\text{O}_4$  stoichiometry,<sup>36</sup> and practical values of  $Q_m$  typically do not exceed  $120 \text{ mAh g}^{-1}$  ( $432 \text{ C g}^{-1}$ ).<sup>47</sup> Hence, the actual material utilization is expected to be higher than 60%.

Except for the somewhat higher anodic charge in system III, attributed to slow faradaic formation of a surface film of the IL on LMO, the values of  $|Q|$  in Figure 4C are mostly comparable among the three systems and indicate that the IL electrolyte does not adversely affect active material utilization. Thus, there is no significant difference in the degree of material utilization between the EC/DEC and the IL electrolyte systems.

The fact that the extents of active material utilization estimated using SSCV data are similar for the EC/DEC and the IL systems (in spite of the more resistive SEI in the latter, as discussed in the following section) can be explained by the observation that Li concentration gradients decrease in the course of cathodic or anodic SSCV scans.<sup>9,34</sup> Because the values of  $Q$  used in the estimation of utilization are cumulative quantities, they are similar for the EC/DEC and the IL systems.

**Electrochemical Impedance Spectroscopy of LMO/IL/Li Cells.** Electrochemical impedance spectroscopy (EIS) was employed to further investigate the SEI films on the active electrode surfaces. The complex nonlinear least-squares

(CNLS) method was used to develop an electrode-equivalent circuit (EEC) model of the LMO-SEI-electrolyte interfaces, as well as to obtain the voltage dependent values of the circuit elements. The circuit model obtained from this analysis is shown in Figure 5 and is commonly found in EIS studies of Li

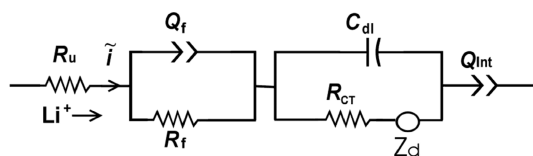


**Figure 5.** Circuit model of Li intercalation/deintercalation at the LMO cathode.

ion battery cathodes.<sup>8,9</sup> This EEC includes impedance elements of both the SEI unit ( $Q_f$  and  $R_f$ ) and the active cathode material (the remaining elements shown on the right of the  $Q_f$ – $R_f$  combination). The common inclusion of the surface film unit in both the electrolyte systems demonstrates that such a film is supported not only by EC/DEC, but also by the IL.

In Figure 5,  $R_u$ ,  $R_f$ , and  $Q_f$  denote the electrolyte resistance, the SEI film resistance, and a constant phase element (CPE) signature of the SEI, respectively.  $Q_f$  accounts for the charge storage characteristics (frequency dispersed capacitance) of the spatially inhomogeneous SEI film, and the impedance contribution of this CPE has the form:  $(1/Y_{of})(j\omega)^{-n}$ , where  $Y_{of}$  and  $n$  are frequency-independent parameters. When  $n = 1$ , the surface film is spatially uniform and the CPE corresponds to a capacitance. In the cathode unit of the EEC,  $R_{ct}$  is the charge transfer resistance of Li extraction/insertion, and  $Z_d$  is the associated impedance of lithium diffusion in the active particle.  $Q_{int}$  is an intercalation CPE and represents the frequency dispersed generalized version of the Li intercalation capacitance.<sup>9</sup>

The measured values of the SEI parameters are plotted in Figure 6 as functions of cell voltages. The results for  $R_u$  are found to be practically voltage independent and are presented in the Supporting Information. According to the CNLS analysis of the data,  $R_u = 0.01$  and  $0.56 \Omega \text{ cm}^2$ , for the EC/DEC and the IL electrolytes, respectively. These results agree well with the corresponding inverse conductivity values of the two electrolytes (at 25 °C) in Figure 1B.

Because the EIS data were recorded on a preconditioned (SEI-formed) cathode under DC equilibrium, any contributions of electrolyte reactions to the observed values of  $R_f$  are insignificant. Under this condition,  $R_f$  represents the mass transfer resistance for the diffusion of  $\text{Li}^+$  in the SEI. This diffusion also promotes compositional heterogeneities inside the particle as indicated by the CPE,  $Q_f$ . In SSCV, the measured electrochemical response of the electrode is a result of averaging these effects over the electrode volume and is manifested in the DC data of Figure 3 in a scan rate dependent manner.

The  $R_f$  values in Figure 6A indicate that the resistance of the SEI formed in the IL system is about an order of magnitude larger than that found for the EC/DEC system. As shown in the Supporting Information,  $R_f$  is proportional to the ratio,  $L_f/D_f$ , where  $L_f$  and  $D_f$  are the average thickness of the SEI layer and the diffusion coefficient of Li in the film, respectively. Therefore, the higher film resistance in the IL case is due to the correspondingly greater SEI thickness and lower diffusion coefficient of  $\text{Li}^+$  as compared to those of the EC/DEC system.

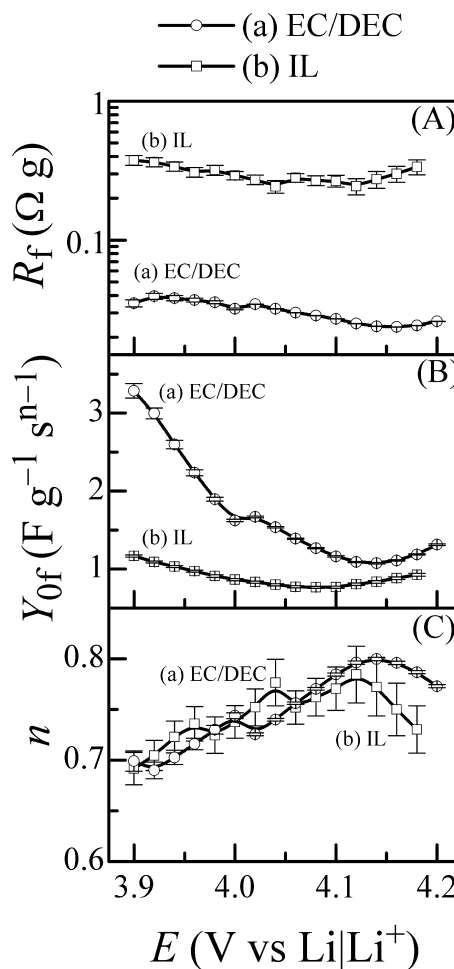


**Figure 6.** CNLS analyzed impedance parameters of cathode-surface films. The symbols denote experimental data obtained from the Nyquist spectra recorded for LMO electrodes in (a) EC/DEC and (b) IL electrolytes containing  $\text{LiTf}_2\text{N}$  (1 M). The lines indicate the overall data trends.

The voltage dependencies of  $R_f$  are mostly insignificant for both electrolytes used and indicate that the SEI layers do not undergo substantial structural changes after their initial formation.

The CPE parameter  $Y_{of}$  for the electrode surface film in EC/DEC decreases as the DC voltages progressively increase in to the region of Li intercalation/deintercalation. This suggests a correspondingly increasing level of spatial homogeneity of the electrode surface. The values of  $Y_{of}$  for the IL also display a somewhat similar trend. As expected based on previously published results,<sup>9,20</sup> the plots for the CPE parameter  $n$  show opposite variations of  $Y_{of}$  in response to variations in the detailed surface morphologies.

In addition to the SEI parameters, the EIS data also provide the kinetic parameters of Li insertion/extraction in/from LMO. Figure 7A plots the EIS-measured charge transfer resistances,  $R_{ct}$ , of the (a) EC/DEC and (b) IL systems. Throughout the voltage range explored here,  $R_{ct}$  is considerably higher for the IL than for EC/DEC.  $R_{ct}$  is inversely proportional to the reaction rate constant,  $k_0$ , of the Li extraction or insertion reaction (assumed to be the same for reactions in both directions).<sup>9</sup> Hence, the  $k_0$  values are significantly lower for the ionic SEI formed by the IL than for the nonionic SEI formed by EC/DEC. This suggests that the presence of ionic groups from



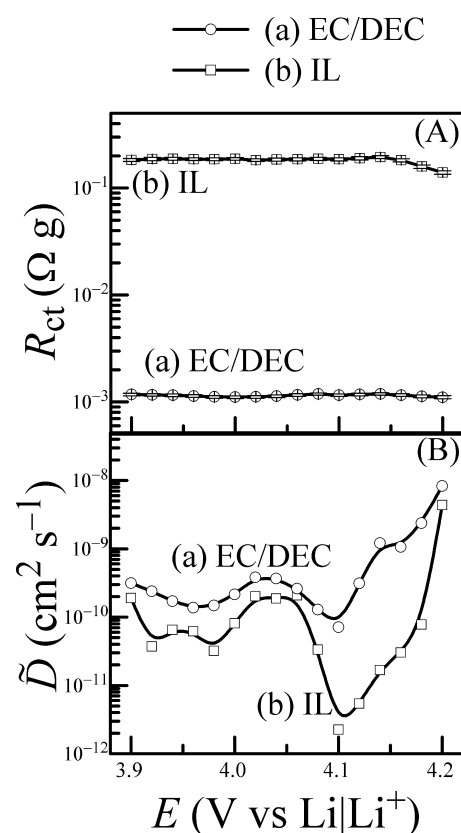


**Figure 7.** (A) Charge transfer resistance and (B) diffusion coefficient for Li transport in LMO, obtained from CNLS analysis of experimental Nyquist data (symbols) recorded in (a) EC/DEC and (b) IL electrolytes containing  $\text{LiTf}_2\text{N}$  (1 M). The lines indicate the overall trends of the data.

the IL in the vicinity of the LMO particle surface results in a decrease in the rate constant of the reaction of lithium with the host lattice.

The chemical diffusion coefficient,  $\tilde{D}$ , of Li inside the host particles is calculated using  $C_{\text{int}}$  from Figure 3 and the EIS-measured parameters,  $R_d$  and  $\omega_d$  of the complex diffusion impedance,  $Z_d$ . Here,  $Z_d = R_d \tanh[(j\omega/\omega_d)^{1/2}]/[(j\omega/\omega_d)^{-1/2}]$ .<sup>8</sup> The detailed steps associated with the evaluation of  $\tilde{D}$  are described in the Supporting Information, and the final results are presented in Figure 7B. The values of  $\tilde{D}$  for the IL system

are smaller than those measured for the EC/DEC system. This observed difference between the two cases again demonstrates the specific effect of chemical composition of the SEI film (ionic vs nonionic) on the properties of the host lattice. The effect of interfacial interactions between the LMO particles and the SEI film would be particularly prominent in cathodes consisting of ball-milled LMO particles because of the large specific surface area of these particles. The values of  $\tilde{D}$  for the two electrolytes are most notably different in the voltage region corresponding to higher values of  $x$ . Therefore, the cathode SEI is expected to display its strongest effects under the conditions of high state of charge.

The relatively low values of  $\tilde{D}$  supported by the IL-generated SEI layer suggest that such a system would be suitable primarily for slow charge–discharge cells. While several types of Li-ion batteries exist in this category<sup>48</sup> and can potentially benefit from the thermal advantage of the IL electrolyte, the cathode charge rates in the presence of IL-generated surface films could be improved further by using SEI-controlling additives in the electrolyte. Since the electrode material plays a crucial role in determining its SEI's  $\text{Li}^+$  transport characteristics,<sup>49</sup> design considerations for rapid-charge cathodes (as well as anodes) should also be coupled with those of the electrolyte and the additives. Experimental strategies for materials engineering of electrolyte additives for such applications have been previously discussed,<sup>50–52</sup> and with additional experiments, can be extended to IL based systems like the one studied here.

**Comparison of Surface Films Formed on LMO in EC/DEC and IL Electrolytes.** The EEC model displayed in Figure 5 indicates that SEI layers can be effectively formed on LMO in both the EC/DEC and the IL electrolytes. Additional substantiation for surface film formation in the IL system is presented in Figure 8. Shown here are the comparative scanning electron microscope (SEM) images of two LMO electrodes, taken after subjecting the electrodes to two full SSCV cycles in the IL and the EC/DEC electrolytes. The surface morphology of the electrode seen in Figure 8A for the IL system is more textured (evidently thicker) due to the presence of a surface film. This comparatively thicker cathode surface film resulting from the IL causes correspondingly higher impedance and slower transport of Li in the IL covered LMO.

SEM images showing pristine (ball-milled) LMO samples have been presented in our earlier work,<sup>20</sup> and can be compared with the data in Figure 8. On the basis of this

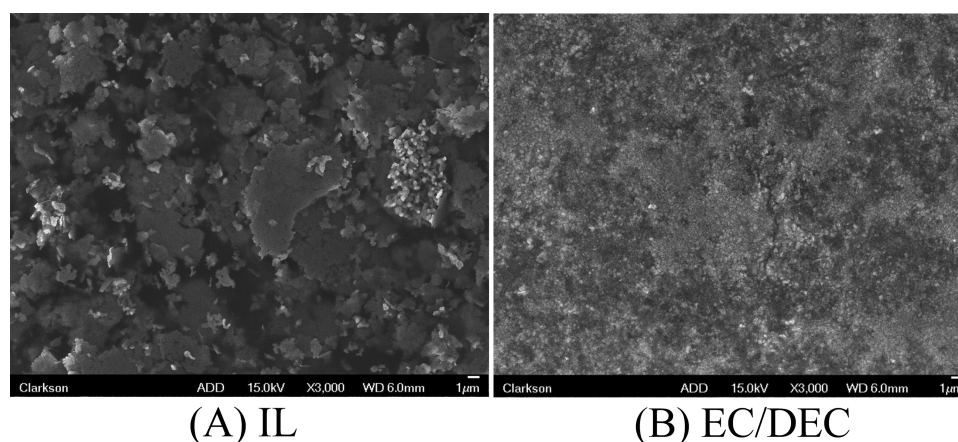


**Figure 8.** Scanning electron micrographs of LMO electrodes used for SSCV experiments involving (A) IL and (B) EC/DEC electrolytes.



consideration, the surface morphology observed here in Figure 8B for the electrode cycled in EC/DEC is not significantly different from that found for the fresh LMO electrodes. This also supports the observation made in Figure 6 regarding the comparative values of  $R_f$  measured in the EC/DEC and IL electrolytes and confirms once again that the EC/DEC generated SEI film of LMO is thinner than the IL supported SEI.

## CONCLUSION

The experiments reported here serve to illustrate an essential set of feasibility criteria for using [mPEG7MeIm][Tf<sub>2</sub>N] as a functional electrolyte in Li ion batteries. The thermophysical properties of this IL are shown to be promising for high temperature applications. Half-cell experiments using cathodes prepared from ball-milled LMO nanoparticles at room temperature indicate that the IL electrolyte is capable of supporting the battery-specific electrochemistry of the cathode. The presence of cationic functional groups from the IL in the SEI has a strong influence on the chemical rate constant for Li extraction/insertion in the host matrix and also on the diffusion coefficient of Li inside the particles. In spite of these mass-transfer limitations encountered in the more viscous IL-based electrolyte, there is practically no difference in the active material utilization (that is, the charge capacity) of cells constructed using the PEGylated IL electrolyte and the conventional EC/DEC electrolyte.

The diffusion of Li through the SEI formed on LMO by [mPEG7MeIm][Tf<sub>2</sub>N] appears to be relatively slow. Hence this specific electrode–IL combination is suitable for stationary applications of Li ion batteries, and especially in those cases where high-temperature stability of the cell becomes a more critical issue than supporting high rates of charge/discharge. Certain high temperature batteries, such as those used for “measure while drilling” applications in oil-fields, often use a different type of Li<sup>+</sup> ion chemistry compared to the case tested in the present study.<sup>53</sup> However, there is another broad class of Li-ion batteries for stationary applications that uses conventional metal oxide cathode chemistries, require charge/discharge at relatively moderate rates (between 1/8-C and 1-C),<sup>54–56</sup> and is often associated with thermal management issues including temperature-induced electrolyte degradation.<sup>54,57</sup> IL electrolytes, similar to that reported here, could potentially cater to a number of the aforementioned operational criteria for such batteries. To quantify the full utility of such IL systems in this regard, it will be necessary to systematically carry out full-cell experiments including careful studies of the electrolyte’s interactions with other cell components such as the anode, the separator, and the current collectors. The exploratory results of cathode–IL interactions presented here can provide the background necessary to set the experimental strategies for such additional studies.

## EXPERIMENTAL DETAILS

**Synthesis of [mPEG7MeIm][Tf<sub>2</sub>N] IL.** Lithium bis-(trifluoromethylsulfonyl)amide (LiTf<sub>2</sub>N, 99%, purchased from Oakwood Products, West Columbia, SC) and all other chemicals (purchased from Sigma-Aldrich, Milwaukee, WI) were used as received. The monomethoxy-terminated PEG, CH<sub>3</sub>O-(CH<sub>2</sub>CH<sub>2</sub>O)<sub>6</sub>CH<sub>2</sub>CH<sub>2</sub>OH, **1** (Scheme 1), was tosylated, and the tosyl ester, **2**, was converted to iodide, **3**, by reaction with NaI, as reported previously.<sup>12</sup> The PEGylated imidazolium iodide, **4**, was obtained by reacting the PEG iodide, **3**, with *N*-methylimidazole. A

solution of LiTf<sub>2</sub>N (55.4 mmol) in 16 g of distilled water was added dropwise to a stirred solution of **4** (36.9 mmol) in 40 g of distilled water. The turbid mixture was stirred at room temperature for 12 h and allowed to settle (for about 1 h) yielding the crude product, [mPEG7MeIm][Tf<sub>2</sub>N] (**5**), as the phase-separated bottom layer. After decanting off the top aqueous layer, the crude product was dissolved in methylene chloride (200 mL) and the solution was thoroughly washed with distilled water (5 × 60 mL). The absence of LiI in the sample was confirmed by the absence of precipitates upon the addition of 10 wt % aq AgNO<sub>3</sub> solution. The methylene chloride was distilled off using a rotary evaporator, and the IL **5** was further dried at 50 °C for 24 h in a vacuum oven, resulting in ~80% yield of [mPEG7MeIm][Tf<sub>2</sub>N]. <sup>1</sup>H NMR (400 MHz) spectra were recorded on a Bruker Advance 400 nuclear magnetic resonance (NMR) spectrometer at ambient temperature in deuterated chloroform (99.8 atom % D, 0.03% v/v tetramethylsilane, TMS).

<sup>1</sup>H NMR (400 MHz, CDCl<sub>3</sub>, δ): 3.31–3.37 (br m, 3H, OCH<sub>3</sub>), 3.63 (br m, 25.3H, CH<sub>2</sub>CH<sub>2</sub>O), 3.84 (t, *J* = 4.4 Hz, 2H, N<sup>+</sup>CH<sub>2</sub>CH<sub>2</sub>O), 3.94 (s, 3H, NCH<sub>3</sub>), 4.35 (t, *J* = 4.2 Hz, 2H, N<sup>+</sup>CH<sub>2</sub>), 7.31–7.42 (br m, 1H, NCH), 7.52 (s, 1H, N<sup>+</sup>CH), 8.83 (s, 1H, N<sup>+</sup>CHN).

Thermogravimetry was performed on a PerkinElmer Pyris 1 analyzer, and the sample temperature was raised to 600 °C at a rate of 15 °C min<sup>−1</sup> under 20 cm<sup>3</sup> min<sup>−1</sup> (standard ambient temperature and pressure) nitrogen purge. The density of the IL was determined to be 1.30 g·cm<sup>−3</sup> at 25 °C using an Ohaus microbalance (model DV215CD), and a 250 μL airtight syringe (Hamilton Co. Inc.).

The IL electrolyte used for electrochemical testing was a 1 M solution of LiTf<sub>2</sub>N in [mPEG7MeIm][Tf<sub>2</sub>N], prepared by mixing LiTf<sub>2</sub>N (0.8804 g) and [mPEG7MeIm][Tf<sub>2</sub>N] (4 g) in dry acetone (5 mL). After stirring the mixture for about 1 h, the acetone was evaporated in a rotary evaporator, and the electrolyte was dried in a vacuum oven at 50 °C for 24 h. For comparison of results, a reference electrolyte of 1 M LiTf<sub>2</sub>N was prepared using conventional organic solvents, which consisted of a blend of EC and DEC (1:1 by volume). All solvents were dried using Type 3 Å molecular sieves (Sigma-Aldrich).

Temperature dependent ionic conductivities of the electrolytes were measured by employing EIS in a two-electrode configuration, using a Teflon test cell containing flat stainless steel electrodes. A 0.01 M KCl solution was used to determine the geometric cell constant of the conductivity cell. DC CV was carried out at a voltage scan speed of 50 mV s<sup>−1</sup> in a three-electrode glass cell containing 0.5 mL of the experimental electrolyte, a GC working electrode (from BASi), a Pt wire reference electrode, and a Pt coil counter electrode (2 mm and 1 mm diameters, respectively, both from Alfa Aesar). A TESTEQUITY 105A environmental chamber, containing a tray of activated silica gel for moisture control, was used to regulate the electrolyte temperatures during all electrochemical measurements.

Cathodes for the LMO/Li cells were prepared using LiMn<sub>2</sub>O<sub>4</sub> spinel powder (CAS no. 12057-17-9, electrochemical grade) purchased from Sigma Aldrich. The powder was ball-milled in a slurry mixture of 10 g LMO, 15 mL of 2-propanol, and cerium-stabilized zirconia beads of 1.2–1.4 mm average diameter, resulting in a bimodal distribution of particles with 300 nm and 1.3 μm average diameters.<sup>20</sup> The particles were dried in a vacuum oven for 12 h at 80 °C. A paste consisting of the ball-milled LMO particles (80 wt %), poly(vinylidene fluoride) (Sigma Aldrich, 7 wt %), and acetylene black (100% compressed, 99.9+%, Alfa Aesar, used 13 wt % in the cathode), thoroughly mixed in *N*-methylpyrrolidone, was applied as a thin film, using a doctor’s blade, on a current collector prepared by sputtering a 1 μm thick gold film on an alumina substrate. The electrode was dried in a vacuum oven for 24 h at 100 °C. A typical cathode was 1.3 cm<sup>2</sup> in area with a film thickness of ~15 μm and contained about 4.0 mg cm<sup>−2</sup> of LMO. Surface morphologies of cycled electrodes were examined by using a JEOL-JSM 6300 scanning electron microscope (SEM).

A three-electrode glass cell was assembled in a humidity controlled glovebox purged with dry argon. Li foils (~1 cm<sup>2</sup> in area) were used as the counter and reference electrodes. Before each electrochemical experiment, the working electrode was soaked in the electrolyte (~4

mL) for 30 min, while ultrahigh purity Ar gas was bubbled through the electrolyte. Each fresh cathode was discharged to 3.4 V to ensure a starting state of charge of zero. SSCV, at 100 and 5  $\mu\text{V s}^{-1}$  scan rates, were performed in the range of 3.4 (or 3.2) to 4.3 V. For potential scans at 100  $\mu\text{V s}^{-1}$  rate, SSCV data were recorded over five cycles. No significant variations were observed beyond the second cycle.

A Solartron 1287A potentiostat/galvanostat EIS was employed to control both the two-electrode and three-electrode electrochemical cells. EIS data were collected using a 15 mV (rms) amplitude AC perturbation voltage of frequencies ranging from 0.01 Hz to 100 kHz. The cathode was subjected to intermittent galvanostatic charging between 3.4 and 4.2 V at a rate of 1/3-C, and Nyquist spectra were recorded at several intermediate open circuit potentials after the electrode current completely dropped to zero. EIS data were analyzed using ZSimpWin to fit to a previously reported EEC model for LMO.<sup>9</sup> The calculated value of each impedance element had an uncertainty of <5%, and the reported values were normalized with respect to the LMO mass in the cathode.

## ■ ASSOCIATED CONTENT

### ■ Supporting Information

Discussion of multiple SSCV scans, the effect of lattice site interactions on voltammetric peak widths of Li intercalation/deintercalation currents, electrochemical stability of monomethoxy-terminated PEG, DC voltage dependent Nyquist plots for LMO-EC/DEC and LMO-IL systems, diffusion resistance of lithium in the SEI film, and impedance parameters of Li transport in LMO. This material is available free of charge via the Internet at <http://pubs.acs.org>.

## ■ AUTHOR INFORMATION

### Corresponding Author

\*E-mail: [samoy@clarkson.edu](mailto:samoy@clarkson.edu).

### Notes

The authors declare no competing financial interest.

## ■ ACKNOWLEDGMENTS

This work was supported by the Army Research Office (Grant No. W911NF-05-1-0339). The authors thank Ramaswamy I. Venkatanarayanan for providing technical assistance with electrolyte preparation and the thermogravimetric measurements.

## ■ REFERENCES

- (1) Lewandowski, A.; Świdarska-Mocek, A. *J. Power Sources* **2009**, *194*, 601–609.
- (2) Yanbao Fu, Y.; Cheng Chen, C.; Chenchen Qiu, C.; Xiaohua Ma, X. *J. Appl. Electrochem.* **2009**, *39*, 2597–2603.
- (3) Sutto, T. E. *J. Electrochem. Soc.* **2007**, *154*, 130–135.
- (4) Zheng, H.; Li, B.; Fu, Y.; Abe, T.; Ogumi, Z. *Electrochim. Acta* **2006**, *52*, 1556–1562.
- (5) Fox, D. M.; Gilman, J. W.; Morgan, A. B.; Shields, J. R.; Maupin, P. H.; Lyon, R. E.; De Long, H. C.; Trulove, P. C. *Ind. Eng. Chem. Res.* **2008**, *47*, 6327–6332.
- (6) Taggougui, M.; Diaw, M.; Carré, B.; Willmann, P.; Lemordant, D. *Electrochim. Acta* **2008**, *53*, 5496–5502.
- (7) Lu, Y.; Das, S. K.; Moganty, S. S.; Archer, L. A. *Adv. Mater.* **2012**, *24*, 4430–4435.
- (8) Goonetilleke, P. C.; Zheng, J. P.; Roy, D. *J. Electrochem. Soc.* **2009**, *156*, A709–A719.
- (9) Zheng, J. P.; Crain, D. J.; Roy, D. *Solid State Ionics* **2011**, *196*, 48–58.
- (10) Van der Ven, A.; Marianetti, C.; Morgan, D.; Ceder, G. *Solid State Ionics* **2000**, *135*, 21–32.
- (11) Wu, F.; Tan, G.; Chen, R.; Li, L.; Xiang, J.; Zheng, Y. *Adv. Mater.* **2011**, *23*, 5081–5085.
- (12) Ganapatibhotla, L. V. N. R.; Zheng, J. P.; Roy, D.; Krishnan, S. *Chem. Mater.* **2010**, *22*, 6347–6360.
- (13) Döbbelin, M.; Azcune, I.; Bedu, M.; de Luzuriaga, A. R.; Genua, A.; Jovanovski, V.; Cabañero, G.; Odriozola, I. *Chem. Mater.* **2012**, *24*, 1583–1590.
- (14) Tang, S.; Baker, G. A.; Zhao, H. *Chem. Soc. Rev.* **2012**, *41*, 4030–4066.
- (15) Lebga-Nebane, J. L.; Rock, S. E.; Franclemont, J.; Roy, D.; Krishnan, S. *Ind. Eng. Chem. Res.* **2012**, *51*, 14084–14098.
- (16) Ganapatibhotla, L. V. N. R.; Wu, L.; Zheng, J.; Jia, X.; Roy, D.; Krishnan, S. *J. Mater. Chem.* **2011**, *21*, 19275–19285.
- (17) Martielli, E.; Galli, G.; Krishnan, S.; Paik, M. Y.; Ober, C. K.; Fischer, D. A. *J. Mater. Chem.* **2011**, *21*, 15357–15368.
- (18) Freemantle, M. *An Introduction to Ionic Liquids*; RSC: Cambridge, UK, 2010; pp 41–64.
- (19) Blesi, M.; Lopes, J. N. C.; Gomes, M. F. C.; Rebelo, L. P. N. *Phys. Chem. Chem. Phys.* **2010**, *12*, 9685–9692.
- (20) Crain, D. J.; Zheng, J. P.; Sulyma, C. M.; Goia, C.; Goia, D.; Roy, D. *J. Solid State Electrochem.* **2012**, *16*, 2605–2615.
- (21) Tang, Z.; Qi, L.; Gao, G. *Solid State Ionics* **2009**, *180*, 226–230.
- (22) Wu, T.-Y.; Wang, H.-C.; Su, S.-G.; Gung, S.-T.; Lin, M.-W.; Lin, C. *J. Taiwan Inst. Chem. Eng.* **2010**, *41*, 315–325.
- (23) Matsumoto, K.; Endo, T. *J. Polymer Sci., Part A: Polym. Chem.* **2011**, *49*, 3582–3587.
- (24) Lu, Y.; Moganty, S. S.; Schaefer, J. L.; Archer, L. A. *J. Mater. Chem.* **2012**, *22*, 4066–4072.
- (25) Javier, A. E.; Patel, S. N.; Hallinan, D. T., Jr.; Srinivasan, V.; Balsara, N. P. *Angew. Chem., Int. Ed.* **2011**, *50*, 9848–9851.
- (26) Mayrand-Provencher, L.; Rochefort, D. *J. Phys. Chem. C* **2009**, *113*, 1632–1639.
- (27) Zhang, J.; Bond, A. M. *Analyst* **2005**, *130*, 1132–1147.
- (28) Moganty, S. S.; Baltus, R. E.; Roy, D. *Chem. Phys. Lett.* **2009**, *483*, 90–94.
- (29) Bard, A. J.; Faulkner, L. R. *Electrochemical Methods: Fundamentals and Applications*; John Wiley: New York, 2001; pp 590–593.
- (30) Zheng, J. P.; Goonetilleke, P. C.; Pettit, C. M.; Roy, D. *Talanta* **2010**, *81*, 1045–1055.
- (31) Hultgren, V. M.; A. Mariotti, A. W.; Bond, A. M.; Wedd, A. G. *Anal. Chem.* **2002**, *74*, 3151–3156.
- (32) Shamsipur, M.; Miran Beigi, A. A.; Teymouri, M.; Pourmortazavi, S. M.; Irandoust, M. *J. Mol. Liq.* **2010**, *157*, 43–50.
- (33) Hayyan, M.; Mjalli, F. S.; Hashim, M. A.; Al Nashief, I. M.; Mei, T. X. *J. Ind. Eng. Chem.* **2013**, *19*, 106–112.
- (34) Zhang, D.; Popov, B. N.; White, R. E. *J. Electrochem. Soc.* **2000**, *147*, 831–838.
- (35) Sun, X.; Yang, X. Q.; Balasubramanian, M.; McBreen, J.; Xia, Y.; Sakaib, T. *J. Electrochem. Soc.* **2002**, *149*, A842–A848.
- (36) Kang, S.-H.; Goodenough, J. B.; Rabenberg, L. K. *Chem. Mater.* **2001**, *13*, 1758–1764.
- (37) Liu, W.; Kowal, K.; Farrington, G. C. *J. Electrochem. Soc.* **1998**, *145*, 459–465.
- (38) Srinivasan, V.; Newman, J. *J. Electrochem. Soc.* **2004**, *151*, A1517–A1529.
- (39) Lu, W.; Belharouak, I.; Liu, J.; Amine, K. *J. Electrochem. Soc.* **2007**, *154*, A114–A118.
- (40) Ma, J.; Wang, C.; Wroblewski, S. *J. Power Sources* **2007**, *164*, 849–856.
- (41) Wang, C.; Kakwan, I.; Appleby, A. J.; Little, F. E. *J. Electroanal. Chem.* **2000**, *489*, 55–67.
- (42) Takami, N.; Hoshina, K.; Inagaki, H. *J. Electrochem. Soc.* **2011**, *158*, A725–A730.
- (43) Ohzuku, T.; Ueda, A. *J. Electrochem. Soc.* **1997**, *144*, 2780–2785.
- (44) Atlung, S.; West, K. *J. Power Sources* **1989**, *26*, 139–159.
- (45) Zhao, K.; Pharr, M.; Vlassak, J. J.; Suo, Z. *J. Appl. Phys.* **2010**, *108*, 073517.
- (46) Jagannathan, K. *J. Electrochem. Soc.* **2009**, *156*, A1028–A1033.
- (47) Manthiram, A.; Kim, J. *Chem. Mater.* **1998**, *10*, 2895–290.

- (48) *Lithium-Ion Batteries: Science and Technologies*; Yoshio, M., Brodd, R. J., Kozawa, A., Eds.; Springer Science: New York, 2009.
- (49) Xu, B.; Qian, D.; Wang, Z.; Meng, Y. S. *Mater. Sci. Eng. R* **2012**, *73*, 51–65.
- (50) Aurbach, D. *J. Power Sources* **2003**, *119–121*, 497–503.
- (51) Xu, J.; Yang, J.; NuLi, Y.; Wang, J.; Zhang, Z. *J. Power Sources* **2006**, *160*, 621–626.
- (52) Aurbach, D.; Talyosef, Y.; Markovsky, B.; Markevich, E.; Zinigrad, E.; Asraf, L.; Gnanaraj, J. S.; Kim, H.-J. *Electrochim. Acta* **2004**, *50*, 247–254.
- (53) Johnson, A. P. In *Encyclopedia of Electrochemical Power Sources*; Garche, J., Dyer, C., Moseley, P., Ogumi, Z., Rand, D., Scrosati, B., Eds.; Elsevier: Amsterdam, 2009; Vol. 4, pp 111–119.
- (54) Viswanathan, V. V.; Choi, D.; Wang, D.; Xu, W.; Towne, S.; Williford, R. E.; Zhang, J.-G.; Liu, J.; Yang, Z. *J. Power Sources* **2010**, *195*, 3720–3729.
- (55) Takei, K.; Ishihara, K.; Kumai, K.; Iwahori, T.; Miyake, K.; Nakatsu, T.; Terada, N.; Arai, N. *J. Power Sources* **2003**, *119–121*, 887–892.
- (56) Iwahori, T.; Mitsuishi, I.; Shiraga, S.; Nakajima, N.; Momose, H.; Ozaki, Y.; Taniguchi, S.; Awata, H.; Ono, T.; Takeuchi, K. *Electrochim. Acta* **2000**, *45*, 1509–1512.
- (57) Vetter, J.; Novák, P.; Wagner, M. R.; Veit, C.; Möller, K.-C.; Besenhard, J. O.; Winter, M.; Wohlfahrt-Mehrens, M.; Vogler, C.; Hammouche, A. *J. Power Sources* **2005**, *147*, 269–281.